Journal of MATERIALS RESEARCH

Invited Feature Paper
DOI:10.1557/s43578-021-00446-5

ULTRA-WIDE BANDGAP MATERIALS, DEVICES, AND SYSTEMS

FOCUS ISSUE

Gas source chemical vapor deposition of hexagonal boron nitride on C-plane sapphire using B_2H_6 and NH_3

Anushka Bansal[1], Xiaotian Zhang[1], Joan M. Redwing[1,2,a)]

[1] Department of Materials Science and Engineering, The Pennsylvania State University, University Park, PA 16802, USA
[2] 2-Dimensional Crystal Consortium (2DCC) Materials Research Institute, The Pennsylvania State University, University Park, PA 16802, USA
[a)] Address all correspondence to this author. e-mail: jmr31@psu.edu

Received: 10 May 2021; accepted: 15 November 2021; published online: 20 December 2021

Chemical vapor deposition (CVD) of hexagonal boron nitride (hBN) using diborane (B_2H_6) and ammonia (NH_3) is reported. The effect of growth conditions on hBN growth rate using continuous vs. flow modulation epitaxy (FME) method is investigated to gain insight into the role of gas-phase chemistry during film deposition. In continuous mode, hBN growth rate decreases with increase in growth temperature, reactor pressure, and decrease in gas velocity. This is attributed to increased gas-phase polymerization of intermediate products such as borazine ($B_3N_3H_6$) which forms high molecular weight species that do not contribute to hBN film growth. Using FME method, the hBN growth rate increases by ~ 25 times compared to continuous mode and exhibits a strong positive dependence on substrate temperature with an activation energy of ~ 61.1 kcal/mol, indicative of a kinetically limited process. The results provide additional insight into the effects of gas-phase reactions on CVD of hBN.

Introduction

Hexagonal Boron Nitride (hBN) is a 2 dimensional (2D), III-nitride wide bandgap semiconductor that has a layered structure very similar to graphite and is often referred to as 'white graphene' owing to its sp^2-hybridized atomic sheets of boron and nitrogen. It is a promising material for emerging applications, including deep ultraviolet (DUV) optoelectronics, neutron detectors, single photon emitters for quantum computing and sensing, etc. [1–10]. Non-metallic substrates such as SiC, α-Al_2O_3, and AlN have been used for large area epitaxial growth of hBN for such applications using molecular beam epitaxy (MBE), chemical vapor deposition (CVD), and metalorganic CVD (MOCVD) methods [11–20].

A variety of precursors are employed for CVD and MOCVD of hBN. Single-source precursors such as ammonia borane (H_3NBH_3) and borazine ($B_3N_3H_6$) are commonly used for hBN deposition, particularly on metal substrates [21]. However, use of these sources typically requires the addition of another nitrogen source (usually NH_3) to control the N/B ratio in deposited hBN films. In addition, $B_3N_3H_6$ is an unstable compound and reacts readily to form low volatility polymers. Chloride-based precursors such as BCl_3 have also been used [22] but require special handling considerations as BCl_3 reacts readily with NH_3 at room temperature to form solid ammonium chloride (NH_4Cl) that can clog outlet tubing and pumps. Carbon-based precursors such as triethyl boron ($B(C_2H_5)_3$, TEB) and trimethyl boron ($B(CH_2)_3$, TMB) have been widely used in MOCVD of hBN but can act as a source of carbon contamination in the films [13, 23–25]. For example, Chugh et. al. identified carbon as a major impurity in hBN films deposited using TEB as the boron precursor forming boron carbide that resulted in large sub-bandgap fluorescence in the range of 1.77–2.25 eV [23].

To circumvent problems with carbon incorporation, diborane (B_2H_6) has been used along with NH_3 for hBN deposition [26, 27]. Yamada et al. did a comparative study using a carbon-based precursor (TEB) and hydride precursor (B_2H_6) and found that significant levels of carbon ($> 10^{20}$ cm^{-3}) and oxygen ($> 10^{19}$ cm^{-3}) impurities were incorporated in the hBN film when TEB was used. The impurity levels were two orders of magnitude lower when hBN was deposited using B_2H_6 [27]. However, B_2H_6 is known to decompose in the gas phase at relatively low temperatures (300–400 °C) [28] forming BH_3 which can further react with NH_3 upstream of the substrate introducing additional intermediate gas-phase compounds during hBN deposition. Growth variables such as temperature, pressure, V/III ratios, and carrier gas flow rates can influence

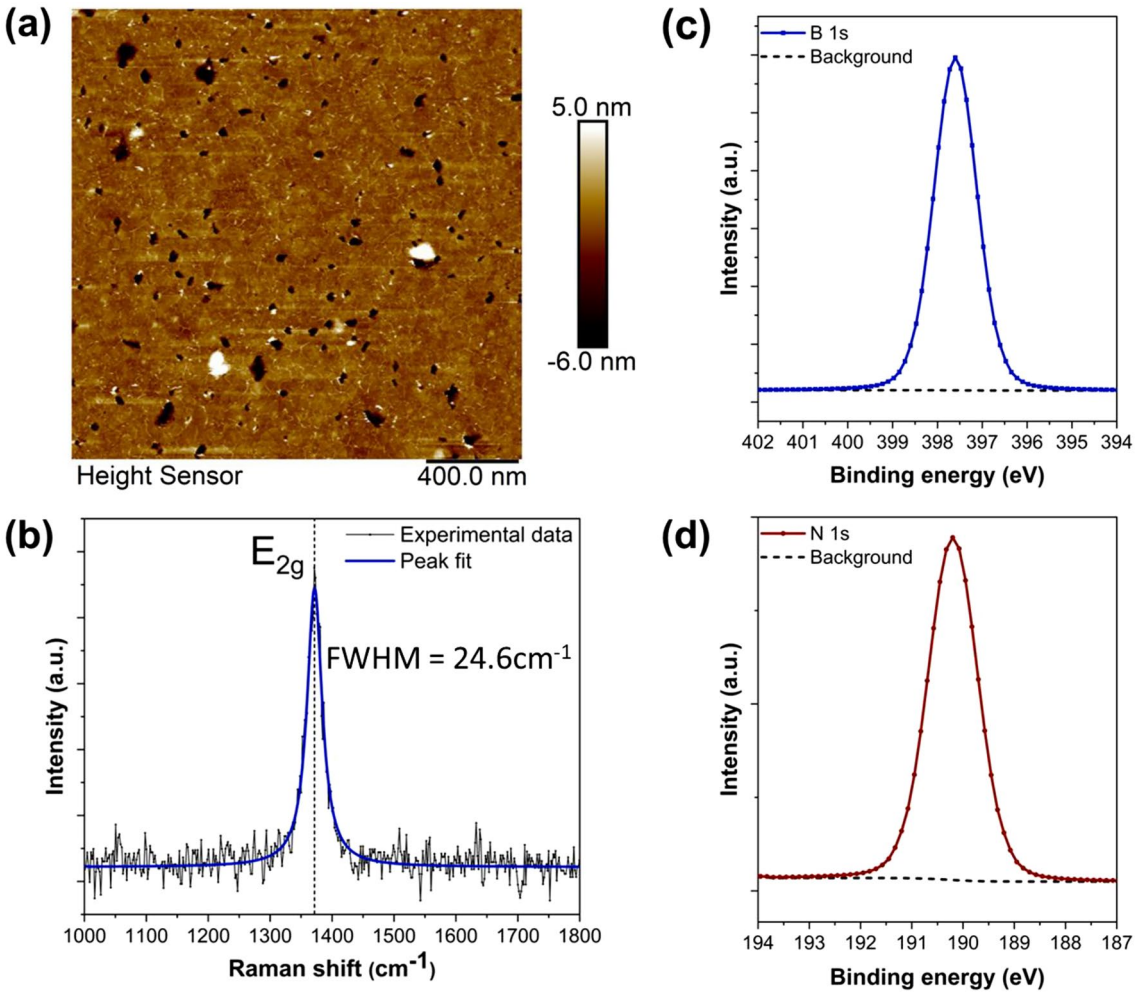

Figure 1: (a) AFM micrograph of the hBN film deposited on C-plane sapphire under the continuous growth mode showing a wrinkled morphology with holes in the film; (b) Raman spectra showing E_{2g} Raman-active mode of hBN as measured along with Lorentzian peak fit to calculate peak position and FWHM; B1s (c) and N1s (d) XPS spectra of the hBN film indicating B–N bonds.

the gas-phase reactions between the precursors, impacting the crystalline quality and growth rate of hBN thin film. A common way to avoid parasitic gas-phase eactions is using flow modulation epitaxy (FME) technique, where different precursors are supplied sequentially, thus, avoiding parasitic gas-phase reactions. Kobayashi et. al. used FME technique for the first time for hBN deposition using TEB and NH_3 and found that the parasitic reactions could be reduced to a large extent using this technique [5, 29]. Another issue is the high temperature (> 1200 °C) required for hBN growth on C-plane sapphire (α-Al_2O_3), as suggested by the early work of Nakamura, et al. At lower deposition temperatures, a disordered form of sp^2-BN, more commonly known as turbostratic BN (tBN) with random stacking sequence between layers of sp^2-BN, or even amorphous BN (aBN) is formed [30, 31]. Such high deposition temperatures required to obtain hBN can increase the extent of gas-phase reactions, impacting the deposition process.

In this paper, we report high-temperature deposition of hBN on C-plane sapphire (α-Al_2O_3) using B_2H_6 and NH_3 as precursors. We focus on comparing the continuous growth mode where the precursors flow simultaneously into the reactor and the FME mode, where precursors are sequentially pulsed into the reactor, to understand the impact of gas-phase reactions on the growth rate of hBN thin films. We report the impact of growth variables such as pressure, V/III ratio, temperature etc. on the hBN growth rate. The results provide additional insights into the role of gas-phase reactions in CVD growth of hBN thin films.

Results and discussion

Continuous growth mode

Figure 1a shows the AFM micrograph of the hBN film obtained using continuous growth mode at a growth temperature of

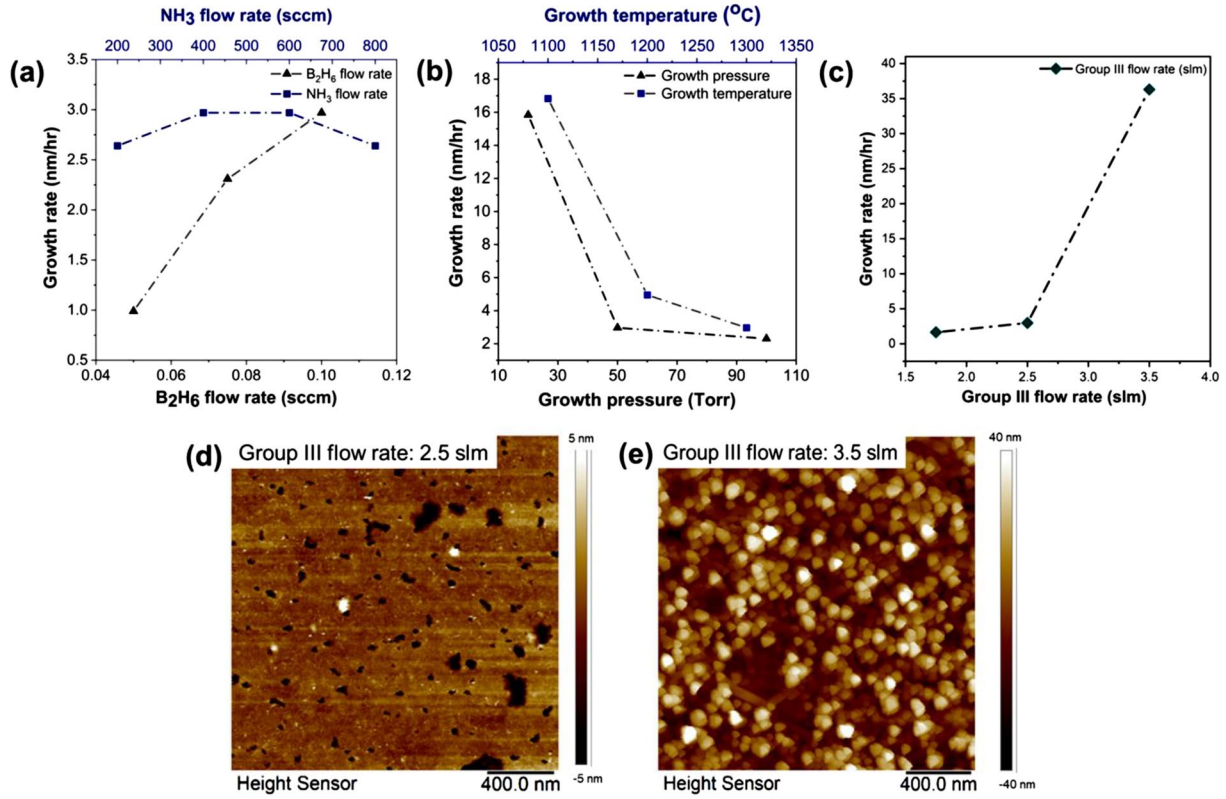

Figure 2: Effect of growth parameters on the hBN growth rate in continuous growth mode; (a) hBN growth rate as a function of B_2H_6 (triangle) and NH_3 (square) flow rates (b) hBN growth rate as a function of growth temperature from 1100 °C to 1300 °C (square) and growth pressure from 20 to 100 Torr (triangle). (c) hBN growth rate as a function of group III H_2 carrier gas flow rate from 1.25 slm to 3.5 slm (diamond) AFM micrographs showing film morphology at group III flow rates of (d) 2.5 slm and (e) 3.5 slm.

1300 °C, reactor pressure of 50 Torr, 2.5 slm of H_2 through the group III inlet cone, and V/III ratio of 2000. A continuousfilm with a thickness of ~ 3 nm and occasional holes is obtained under these conditions, consistent with previous reports by Snure et. al. [24] for hBN deposited on sapphire using TEB and NH_3. The average roughness of the hBN film is 0.7 nm, and it also exhibits wrinkles that arise due to coefficient of thermal expansion (CTE) mismatch between hBN and α-Al_2O_3. hBN has an in-plane negative thermal expansion coefficient of -2.7×10^{-6} K^{-1}, while α-Al_2O_3 has a positive coefficient of 5.0×10^{-6} K^{-1} [20]. One of the possible reasons for occasional holes in the film is etching of the α-Al_2O_3 surface in the H_2/ NH_3 growth environment due to slow hBN growth rate (~ 3 nm/h) using continuous mode of growth. Figure 1b shows E_{2g} Raman-active mode of obtained hBN at 1371.5 cm^{-1} with a FWHM of 24.6 cm^{-1}. The peak is shifted to higher wavenumbers (blue shift) than the reported value for stress-free hBN film/ bulk hBN, which has a peak position at ~ 1365 cm^{-1} [32, 33]. This is due to residual compressive stress in the hBN film arising from CTE mismatch between the film and the substrate, as discussed previously. Figure 1c and d shows B 1s and N 1s peaks at binding energies of 397.6 eV and 190.2 eV, respectively, consistent with B–N bonding. From XPS analysis, the B/N is measured to be 0.96 indicating the presence of N vacancies in the obtained hBN film.

To investigate the role of gas-phase chemistry in continuous growth mode of hBN deposition, the B_2H_6 or NH_3 flow rates were varied while keeping the flow rate of the other precursor (NH_3 and B_2H_6, respectively) constant. As the B_2H_6 flow rate increases, the growth rate increases almost linearly; however, with increasing NH_3 flow rate, the growth rate does not vary (Fig. 2a). This indicates that NH_3 is present in excess during the growth process while the growth rate is limited/ controlled by the supply of B_2H_6 in the reactor. The effect of growth variables such as temperature, pressure, and group III inlet carrier gas flow rate on the growth rate was also measured. As seen in Fig. 2b, with an increase in growth pressure from 20 to 100 Torr, the growth rate decreases sharply from 16 to 2 nm/h, respectively, at a growth temperature of 1300 °C. Moreover, as the growth temperature increases, the growth rate drops significantly from 17 nm/h at 1100 °C to 3 nm/h at 1300 °C (Fig. 2b) at a constant reactor pressure of 50 Torr. The H_2 carrier gas through the group III cone (Fig. 2c) was increased from 1.75 slm to 3.5 slm to increase

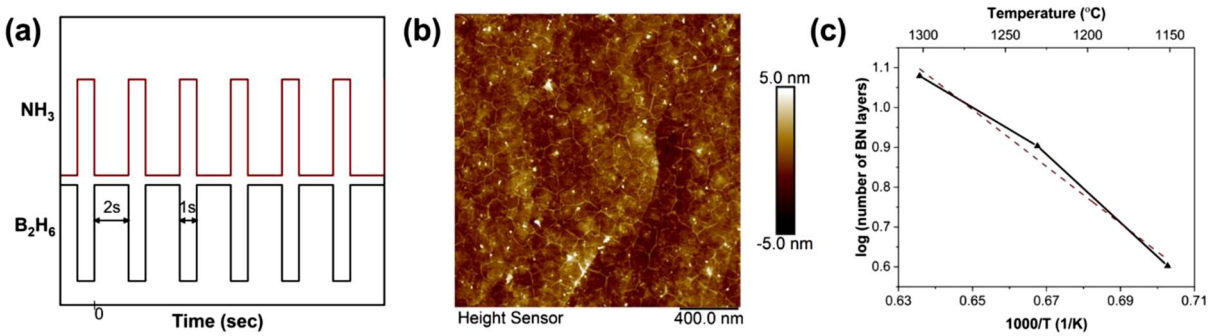

Figure 3: (a) Schematic of the FME growth mode showing B_2H_6 and NH_3 pulses for 2 s and 1 s, respectively. (b) AFM image showing typical film morphology of obtained hBN using FME. (c) Natural logarithm of number of hBN layers (growth rate) as a function of 1/*T*. The slope of this curve indicates the activation energy for the proces.

the gas velocity at a constant growth temperature of 1300 °C and reactor pressure of 50 Torr. In this case, the growth rate increases significantly from 2 to 37 nm/h. The dependencies of hBN growth rate on reactor pressure, growth temperature, and group III inlet gas flow rate are consistent with a growth process that is controlled by gas-phase reactions between precursors. Figure 2d and e shows the morphology of the hBN films obtained with varying group III flow rates of 2.5 slm and 3.5 slm, respectively, indicating that the surface morphology changes from relatively smooth films to a surface consisting of nanoscale islands as the growth rate/film thickness increases with higher group III flow rate.

Prior studies have considered various pathways for gas-phase reactions between B_2H_6 and NH_3 leading to the formation of hBN. For example, Gomez-Aleixandre et al. proposed that depending on the $[NH_3]/[B_2H_6]$ ratio, different intermediate compounds can form [34, 35]. If B_2H_6 is present in excess, aminodiborane ($B_2H_5NH_2$) is formed. However, in a medium with an excess of NH_3 (or low B_2H_6 concentration), $B_2H_5NH_2$ may react with other NH_3 molecules, producing different adduct compounds and aminoborane (H_2BNH_2), which further rearranges to form borazine ($B_3N_3H_6$, a ring compound) as shown below in Eq. (1). On further heating, $B_3N_3H_6$ undergoes progressive loss of hydrogen until BN is finally obtained. Therefore, for simplification, we will assume that among many gas-phase reactions in the current setup, the intermediate compounds that ultimately lead to hBN are $B_2H_5NH_2$ and $B_3N_3H_6$.

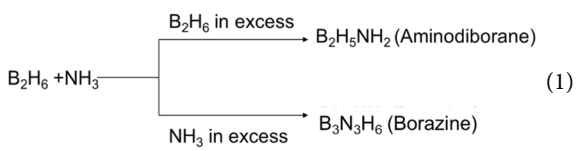

(1)

As the extent of gas-phase reactions increases, $B_3N_3H_6$ molecules can undergo polymerization forming high molecular weight species that do not decompose to form hBN film on the substrate but instead form solid clusters in the gas phase that can be entrained in the gas streamlines and swept away from the substrate surface. Such residual particles were observed as white powder, downstream of the substrate in the reactor chamber after the growth. These results indicate that at higher growth temperature/growth pressure and at lower group III H_2 carrier gas flow rate, gas-phase reactions are extensive leading to high molecular weight polymeric clusters that remove B and N precursors from the growth ambient resulting in a significantly reduced hBN growth rate on the substrate surface.

Flow modulation epitaxy

To suppress the gas-phase reactions, FME mode was adopted to deposit hBN thin film on C-plane sapphire substrate. In this technique, precursors were supplied sequentially, which reduces the chances for gas-phase reactions to occur. For the FME mode, growth was performed at 1300 °C, at a growth pressure of 50 Torr and V/III ratio of 2000. B_2H_6 and NH_3 were sequentially pulsed for 2 s and 1 s, respectively, with no additional purge step as shown in Fig. 3a. The number of pulses for B_2H_6 was adjusted so that it was equivalent to the total growth time used in the continuous growth mode to compare the growth rates between the two techniques. The growth rate achieved through FME was ~ 25 times higher than obtained using continuous mode of growth (~ 3 nm/h in continuous mode compared to ~ 75 nm/h in FME mode). Figure 3b shows a representative AFM image of the surface morphology of an hBN film deposited using FME with a growth time of 3 min (~ 3 nm thick hBN) using the growth conditions mentioned above. The films were continuous with a wrinkled morphology and no apparent holes in the film. This is likely due to the higher growth rate of the FME mode which covered the α-Al_2O_3 surface faster with hBN, thus, preventing substrate etching under NH_3/H_2 environment. The growth rate of hBN films using FME was measured at different growth temperatures. As shown in Fig. 3c, the growth rate increases

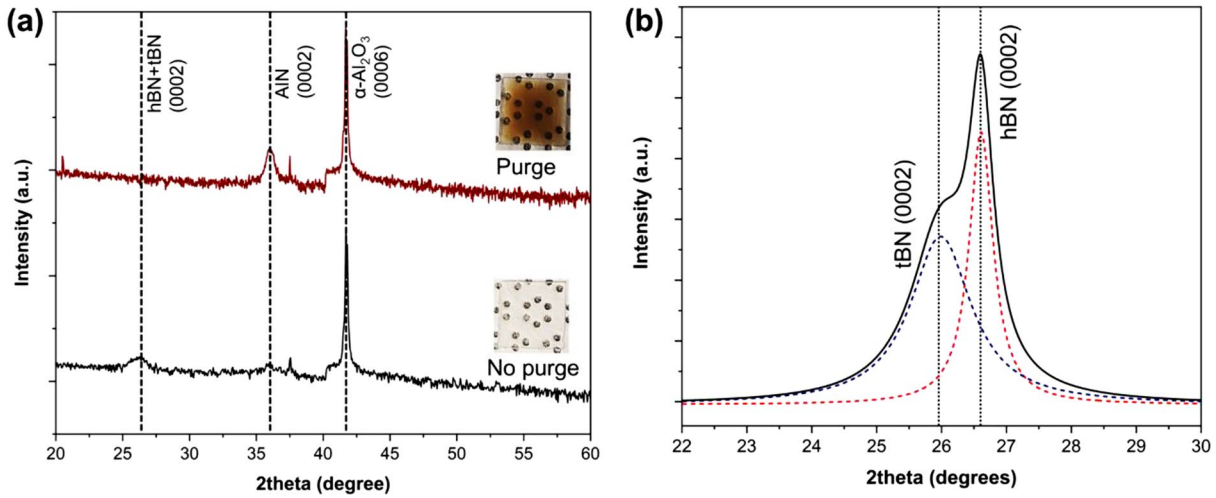

Figure 4: (a) XRD theta-2-theta scans for a set of hBN deposited using FME with no purge between B_2H_6 and NH_3 pulse (black curve) and purge after both B_2H_6 and NH_3 pulses (red curve) along with optical images of the samples deposited in each case (b) High resolution XRD theta-2θ scan to identify phases of sp^2-BN obtained.

with increasing growth temperature for FME in contrast to the continuous flow mode where a decrease in growth rate with increasing temperature was obtained (Fig. 2b).

In a typical CVD growth process, the deposition rate of the films on the substrate may be limited by chemical reactions (kinetically limited) or by mass transport of precursors to the substrate surface. As shown in Fig. 3c, the temperature dependence of the hBN growth rate can be fit to an Arrhenius form (log (deposition rate) v/s 1/temperature) indicating that the deposition is kinetically limited. An activation energy of 61.1 kcal/mol was calculated from the linear fit, which is similar to that reported for MOCVD growth of hBN on an AlN substrate using TEB and NH_3 [36]. In contrast, the growth rate decreased with increasing temperature for continuous mode growth (Fig. 2b). Various intermediate steps could be kinetically limiting the growth rate during the BN deposition process, in the FME growth mode. It is assumed that BH_3 (produced by B_2H_6 decomposition) will react readily in the gas phase with NH_3 to form ammonia borane (BH_3-NH_3). Ammonia borane can then undergo a series of dehydrocoupling reactions which ultimately lead to the formation of borazine ($B_3N_3H_6$) and H_2. Kumar et. al. proposed two reaction pathways associated with the formation of $B_3N_3H_6$ from ammonia borane which have high activation energies in the range of 45–50 kcal/mol [37]. Consequently, the 61.1 kcal/mol that we measure experimentally may be associated with the formation of borazine. Alternatively, the activation energy may also be associated with reactions involving subsequent H_2 loss from borazine to ultimately form BN. A detailed study of the gas-phase and surface reactions is required to fully understand the reaction pathways involved with BN formation to identify the rate limiting step.

While FME with alternating precursor flow minimizes gas-phase reactions, there is still a possibility of intermixing of the precursors since the gas concentration does not change abruptly between pulses. Therefore, to significantly reduce the possibility of gas-phase reactions, a 15 s H_2 purge step was introduced in between precursor pulses to enable one precursor to flush out of the system before the next precursor was introduced. Through XRD analysis (Fig. 4a), it was found that crystalline hBN forms only in the case where there was no purge step in between B_2H_6 and NH_3 pulses. When a H_2 purge step is included after both the B_2H_6 and NH_3 pulses, XRD peak corresponding to hBN was not observed; however, a distinct AlN peak was observed indicating that NH_3 interacted with α-Al_2O_3 surface instead to form AlN. Moreover, the hBN film obtained with no purge step in between is transparent in color indicating an almost stoichiometric film as observed using XPS as well. In the case of the purge step in between the precursor pulses, the deposited film is yellow in color, which indicates a nonstoichiometric/defective film. Note that the growth time was adjusted such that the films are ~ 100 nm thick to be able to successfully collect XRD data, which otherwise is difficult due to the light B and N atoms. These results demonstrate that some level of gas-phase intermixing of B_2H_6 and NH_3 is necessary for crystalline hBN growth, which suggest that gas-phase reactions also play an important role in hBN growth using FME.

Chubarov et. al. demonstrated that at low growth temperatures, a mixture of two phases of sp^2-BN is obtained. To identify the disorder (fraction of hBN vs tBN phase) in films deposited in this case, high resolution XRD scans were performed on the

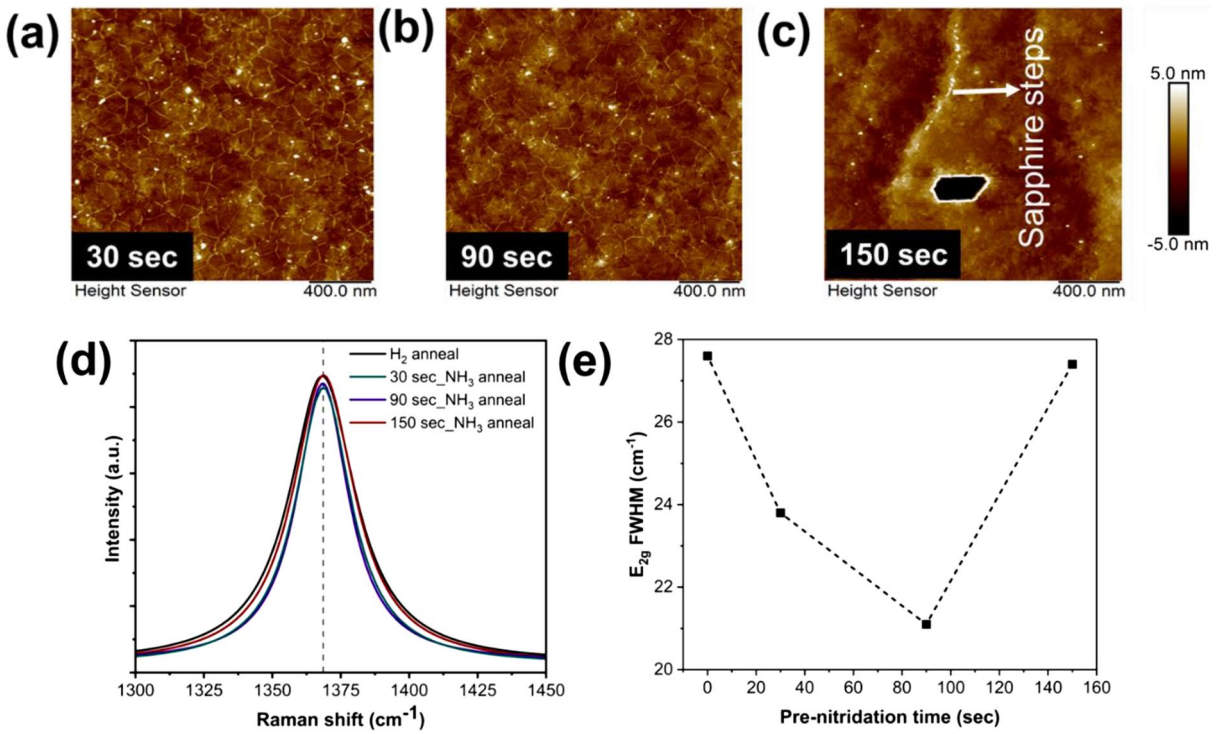

Figure 5: (a), (b) and (c) are AFM images showing surface morphology of the hBN film as a function of pre-nitridation time. Prolonged exposure to NH_3 prior to hBN deposition causes holes in the film (c) as observed in the continuous growth mode. (d) Raman spectra showing E_{2g} active mode for hBN as function of nitridation time (e) Raman E_{2g} mode peak FWHM as a function of pre-nitridation time.

hBN sample with no purge steps in between. As can be seen from Fig. 4b, two peaks were fitted in the collected data: 26.6° corresponding to hBN and 25.9° for tBN, indicating that a mixture of two phases (hBN and tBN) were obtained using FME [38]. Thus, we suspect that to obtain phase pure hBN, an even higher temperature is required such that the layers are arranged in order forming pure hBN, as observed in previous reports [17, 18].

Previous reports have shown that pre-nitridation of the α-Al_2O_3 surface improves the quality of the hBN film obtained [18, 24]. Thus, to understand the impact of NH_3 treatment on the surface morphology evolution of hBN films deposited using FME, α-Al_2O_3 nitridation was done prior to hBN deposition at 1300 °C using 200 sccm of NH_3 for times ranging from 30 to 150 s. As shown in Fig. 5a–c, the hBN film obtained are continuous with a wrinkled morphology in all cases (30 s, 90 s and 150 s). However, with pre-nitridation time of 150 s, holes start to appear in the film due to prolonged exposure to NH_3 and H_2 under the FME growth conditions, similar to that observed in the case of continuous growth mode. The Raman-active E_{2g} mode for hBN was observed at 1368.8 cm^{-1} for H_2 annealed as well as pre-nitridated hBN samples (Fig. 5d, e). The peak is at higher wavenumbers than obtained for hBN bulk crystal at 1365 cm^{-1} due to residual compressive stress in the film left after deposition, as observed in the continuous growth mode as well. With an increase in pre-nitridation time from 0 to 90 s, the FWHM decreases form 27.6 cm^{-1} to 21.1 cm^{-1} indicating that pre-nitridation helps in improving film quality, however for a pre-nitridation time of 150 s, the FWHM increases to 27.4 cm^{-1} indicating that with further nitridation, the film quality worsens which is corroborated with holes observed in the film as seen in Fig. 5(c).

Conclusion

In summary, continuous growth mode vs FME mode was compared to understand the impact of gas-phase reactions between B_2H_6 and NH_3 precursors on hBN deposition on C-plane sapphire. In continuous mode of deposition, the growth rate decreases with an increase in temperature, reactor pressure and a decrease in gas velocity, consistent with a process in which gas-phase pre-reactions play an important role. It was found that the growth rate increases by 25× under FME mode as compared to continuous mode. Furthermore, in the case of FME Mode with sequential precursor pulses, the growth rate increases as a function of temperature indicating a kinetically limited process. However, when a purge step was added between precursor pulses in FME mode, crystalline BN

did not deposit indicating that some degree of gas-phase mixing is required for hBN deposition.

The results are explained in terms of gas-phase chemistry involving the formation of ammonia borane (BH_3-NH_3) which can react in the gas phase to form cyclic borazine ($B_3N_3H_6$). In continuous mode, borazine can polymerize in the gas phase leading to the formation of high molecular weight species which do not contribute to hBN growth. However, when FME is employed, the extent of gas-phase reactions is reduced resulting in a higher concentration of borazine reaching the substrate surface. When a purge step is added between precursor pulses, the formation of borazine is suppressed and crystalline hBN does not deposit. Further work including computational modeling is required to completely understand the gas-phase chemistry between B_2H_6 and NH_3 and the reaction pathways that lead to the formation of hBN.

Experimental methods

An inductively heated vertical cold wall MOCVD reactor originally designed for group III-nitride epitaxy (GaN, AlN, InN) at substrate temperatures up to 1175 °C was used for hBN deposition. The reactor includes two concentric conical quartz inlets to separate the flow of group III and group V precursors (Fig. 6a). The substrate (up to 2″ diameter) sits on an inductively heated SiC-coated graphite susceptor supported by a quartz rod that includes a thermocouple to measure the temperature of the bottom of the susceptor that is in contact with the quartz shaft (Fig. 6b). In order to achieve higher substrate temperatures (> 1200 °C) required for hBN growth, the susceptor and quartz support rod were redesigned; since with the current design, quartz begins to soften above 1200 °C (dotted line in Fig. 6a was the initial length of the susceptor). The susceptor design had to be modified to elongate vertically (beyond the dotted line in Fig. 6a) such that that the point of contact between the susceptor bottom and quartz shaft was maintained well below 1200 °C, while the susceptor surface temperature was ~ 1500 °C required for hBN deposition. To achieve these specifications, a computational fluid dynamics (CFD) model of heat transfer in the MOCVD reactor was developed using the commercial software COMSOL Multiphysics 5.3 based on the thermal-fluid environment and inductive coupling. A 2D-axisymmetric model and corresponding mesh were used due to the axial symmetry of the reactor to reduce the computational complexity of the simulations. The calculation of gas transport in the reactor was based on the solution of coupled partial differential equations for the conservation of momentum, energy, and mass using the Multiphysics module non-isothermal flow from the software in which the calculations of both laminar flow and heat transfer in fluid share the same material properties. Considering H_2 as the main component of the gas mixture, compressible form of the Naiver-Stokes and continuity equations were applied to maintain mass and momentum conservation in the simulations. Part of the non-isothermal flow calculation also included the water in the water jacket with a standard flow rate of 1 gal/min and mean molar mass of 0.018 kg/mol. Simultaneously, the heating source of the susceptor was calculated from the inductive effect between the outside coils and the inside graphite-based susceptor by introducing magnetic field physics to the system. In this case, the copper coils were tuned with five turns, 11 mm in diameter, 6×10^7 S/m conductivity and 27 kW of input power. In addition to the heat conduction and convection, heat radiation was also taken into consideration. Surface-to-surface radiation was included under the assumption of constant wavelength dependence of emissivity and unity transparent media refractive index. The opacity of the system components was based on the real situation. Based on the predicted temperature profile using this model (Fig. 6b, c), a susceptor length of 10 cm above the quartz shaft was required in order to maintain a temperature of 900 °C at the susceptor-quartz interface for a susceptor surface temperature of ~ > 1500 °C. Thus, the susceptor and shaft design were modified successfully to be able to safely reach a temperature of ~ 1500 °C at the top surface of the susceptor.

On-axis C-plane sapphire substrates [(0001) α-Al_2O_3 from Cryscore Optoelectronics], diced to 1×1 cm^2 were used for hBN deposition. Prior to growth, the substrates were cleaned of organic residues via ultrasonication in acetone and isopropyl alcohol for 10 min each, 40 min immersion in commercial Piranha solution (Nano-Strip, KMG Electronic Chemicals) followed by multiple rinses in de-ionized water. B_2H_6 (2% and 0.2% diluted in H_2) and NH_3 were used as precursors for B and N, respectively, with H_2 as the carrier gas. For the study using continuous flow of precursors during growth, the reactor pressure was varied from 20 to 100 Torr and the group III carrier gas flow rate was varied from 1.25 slm to 3.5 slm to investigate the extent of parasitic gas-phase reactions during hBN deposition. B_2H_6 flow rate was varied from 0.05 sccm to 0.1 sccm while NH_3 flow rate was held constant at 200 sccm, thus varying the V/III ratio from 2000 to 4000. Additional studies were carried out in which B_2H_6 was kept constant at 0.1 sccm while NH_3 was varied from 200 to 800 sccm, thus varying the V/III ratio from 2000 to 8000. For the studies using FME growth mode, B_2H_6 pulse time was kept at 2 s while the NH_3 pulse time was kept at 1 s. In some cases, a H_2 purge step of 15 s was introduced between the precursor pulses to further minimize the extent of precursor mixing and gas-phase reactions. For continuous mode as well as FME mode, the substrate temperature was varied from 1100 to 1300°C.

The hBN film thickness/growth rate was measured using Fourier Transform Infrared (FTIR) Spectroscopy. The measurements were performed on a vertex 70 spectrometer (Bruker

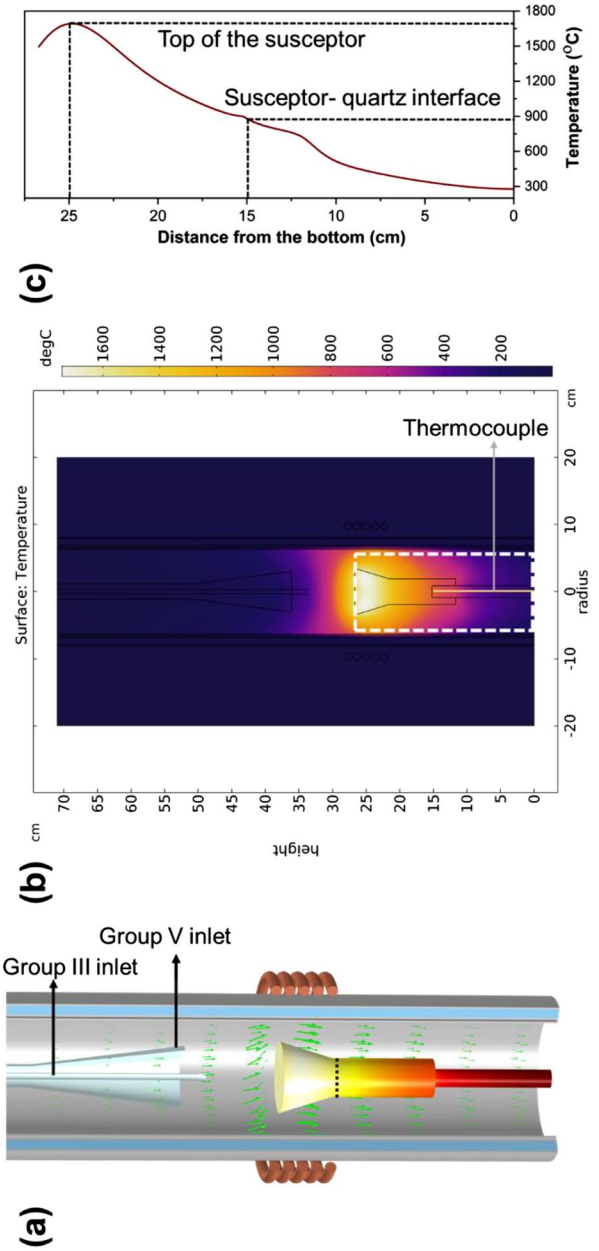

Figure 6: (a) Schematic of the RF inductively heated cold wall reactor design with two cone-shape quartz inlets (group III and group V) and vertically elongated susceptor such that top of the susceptor surface reaches 1500 °C but the point of contact between susceptor and quartz shaft is below 1200 °C. The dotted line represents the length of the graphite susceptor in the original system design (b) 2D model of the temperature distribution profile with 27 kW input power; the yellow line represents a thermocouple used to measure temperature and (c) a temperature line profile vertically along the center of the susceptor in the boxed area shown in (b) indicating the temperature at the top of the susceptor surface and point of contact between susceptor and quartz support shaft.

Optics, Bellerica MA) equipped with a liquid nitrogen cooled narrow band mercury cadmium telluride detector. IR spectra was acquired in specular reflection geometry using a Veemax variable angle accessory (pike tech, cottonwood WI) at an incident angle of 30 degrees. A total of 100 scans were averaged at 6 cm^{-1} resolution per spectrum and reflectance was calculated by referencing to bare C-plane α-Al_2O_3. The surface morphology of the samples was analyzed by atomic force microscopy (AFM) using peak-force tapping mode on a Bruker Dimension Icon Atomic Force Microscope system. OLTESPA-R3 air probe AFM tips with a nominal tip radius of ~7 nm and spring constant of 2 N/m was used for the measurements.

X-ray diffraction (XRD) patterns were collected at 45 kV and 40 mA from 10° to 70° 2-theta(2θ) on a Panalytical X'Pert Pro MPD X-ray diffractometer equipped with Cu K-alpha radiation, 0.04 rad. Soller slits, a 10 mm beam mask, 1/4° and 1/2° divergence and anti-scatter slits respectively on the incident side, and a PIXcel detector operating in scanning line mode with a 1/2° anti-scatter slit, 0.04 rad Soller slit, and a 0.2 mm Ni K-betha filter on the divergent side. Raman spectra were taken using Horiba LabRam HR Evolution VIS–NIR Raman system with a 532 nm laser at 5 mW laser power.

Acknowledgments

Financial support for this work was provided by the National Science Foundation (NSF) through the 2D Crystal Consortium–Materials Innovation Platform (2DCC-MIP) under NSF cooperative agreement DMR-1539916 and DMR-1808900.

Data availability

The data that support the findings of this study are available from the corresponding author upon reasonable request.

Declarations

Conflict of interest On behalf of all authors, the corresponding author states that there is no conflict of interest.

References

1. K. Watanabe, T. Taniguchi, H. Kanda, Nat. Mater. **3**, 404 (2004)
2. K. Watanabe, T. Taniguchi, T. Niiyama, K. Miya, M. Taniguchi, Nat. Photonics **3**, 591 (2009)
3. F. Withers, O. Del Pozo-Zamudio, A. Mishchenko, A.P. Rooney, A. Gholinia, K. Watanabe, T. Taniguchi, S.J. Haigh, A.K. Geim, A.I. Tartakovskii, K.S. Novoselov, Nat. Mater. **14**, 301 (2015)
4. Y. Kobayashi, K. Kumakura, T. Akasaka, T. Makimoto, Nature **484**, 223 (2012)
5. Y. Kobayashi, T. Akasaka, J. Cryst. Growth **310**, 5044 (2008)
6. Y. Kobayashi, T. Akasaka, T. Makimoto, J. Cryst. Growth **310**, 5048 (2008)
7. T.Q.P. Vuong, G. Cassabois, P. Valvin, E. Rousseau, A. Summerfield, C.J. Mellor, Y. Cho, T.S. Cheng, J.D. Albar, L. Eaves, C.T. Foxon, P.H. Beton, S.V. Novikov, B. Gil, 2D Mater. **4**(2), 021023 (2017)
8. M.G. Silly, P. Jaffrennou, J. Barjon, J.-S. Lauret, F. Ducastelle, A. Loiseau, E. Obraztsova, B. Attal-Tretout, E. Rosencher, Phys. Rev. B **75**, 85205 (2007)
9. K. Ahmed, R. Dahal, A. Weltz, J.J.Q. Lu, Y. Danon, I.B. Bhat, Appl. Phys. Lett. **110**, 023503 (2017)
10. R. Bourrellier, S. Meuret, A. Tararan, O. Stephan, M. Kociak, L.H.G. Tizei, A. Zobelli, NANO Lett. **16**, 4317 (2016)
11. C.L. Tsai, Y. Kobayashi, T. Akasaka, M. Kasu, J. Cryst. Growth **311**, 3054 (2009)
12. R. Page, J. Casamento, Y. Cho, S. Rouvimov, H.G. Xing, D. Jena, Phys. Rev. Mater. **3**, 1 (2019)
13. Q. Paduano, M. Snure, D. Weyburne, A. Kiefer, G. Siegel, J. Hu, J. Cryst. Growth **449**, 148 (2016)
14. V. Sorkin, Y. Cai, Z. Ong, G. Zhang, Y.W. Zhang, Crit. Rev. Solid State Mater. Sci. **42**, 1 (2017)
15. K. Ahmed, R. Dahal, A. Weltz, J.J.Q. Lu, Y. Danon, I.B. Bhat, Mater. Res. Express **4**, 015007 (2017)
16. M. Chubarov, H. Pedersen, H. Högberg, Z. Czigany, A. Henry, CrystEngComm **16**, 5430 (2014)
17. M. Chubarov, H. Pedersen, H. Högberg, J. Jensen, A. Henry, Cryst. Growth Des. **12**, 3215 (2012)
18. M. Chubarov, H. Pedersen, H. Hogberg, A. Henry, Z. Czigany, J. Vac. Sci. Technol. A **33**(6), 061520 (2015)
19. A. Rice, A. Allerman, M. Crawford, T. Beechem, T. Ohta, C. Spataru, J. Figiel, M. Smith, J. Cryst. Growth **485**, 90 (2018)
20. X. Li, S. Sundaram, Y. El Gmili, T. Ayari, R. Puybaret, G. Patriarche, P.L. Voss, J.P. Salvestrini, A. Ougazzaden, Cryst. Growth Des. **16**, 3409 (2016)
21. J. Li, C. Zhang, B. Li, F. Cao, S.W.-S. and C. Technology, and undefined 2011, Elsevier (n.d.).
22. N. Umehara, A. Masuda, T. Shimizu, I. Kuwahara, T. Kouno, H. Kominami, K. Hara, Iopscience.Iop.Org **55**, (2016).
23. N. Mendelson, D. Chugh, J.R. Reimers, T.S. Cheng, A. Gottscholl, H. Long, C.J. Mellor, A. Zettl, V. Dyakonov, P.H. Beton, S.V. Novikov, C. Jagadish, H.H. Tan, M.J. Ford, M. Toth, C. Bradac, I. Aharonovich, Nat. Mater. **20**(3), 321–328 (2020)
24. M. Snure, Q. Paduano, A. Kiefer, J. Cryst. Growth **436**, 16 (2016)
25. D. Chugh, J. Wong-Leung, L. Li, M. Lysevych, H.H. Tan, C. Jagadish, 2D Mater. **5**, 1 (2018)
26. H. Yamada, S. Inotsume, N. Kumagai, T. Yamada, M. Shimizu, Phys. Status Solidi **257**, 1900318 (2020)
27. H. Yamada, S. Inotsume, N. Kumagai, T. Yamada, M. Shimizu, Phys. Status Solidi **218**, 2000241 (2021)
28. D.R. Lamborn, D.W. Snyder, X.X. Xi, J.M. Redwing, J. Cryst. Growth **299**, 358 (2007)
29. Y. Kobayashi, T. Nakamura, T. Akasaka, T. Makimoto, N. Matsumoto, J. Cryst. Growth **298**, 325 (2007)
30. K. Nakamura, J. Electrochem. Soc. **133**, 1120 (1986)
31. M. Chubarov, H. Pedersen, H. Högberg, V. Darakchieva, J. Jensen, P.O.Å. Persson, A. Henry, Phys. Status Solidi **10**, 397 (2011)
32. R.V. Gorbachev, I. Riaz, R.R. Nair, R. Jalil, L. Britnell, B.D. Belle, E.W. Hill, K.S. Novoselov, K. Watanabe, T. Taniguchi, A.K. Geim, P. Blake, Small **7**, 465 (2011)
33. Y. Kubota, K. Watanabe, O. Tsuda, T. Taniguchi, Science (80-) **317**, 932 (2007)
34. C. Gómez-Aleixandre, D. Díaz, F. Orgaz, J.M. Albella, J. Phys. Chem. **97**, 11043 (1993)

35. C. Gomez-Aleixandre, A. Essafti, M. Fernandez, J.L.G. Fierro, J.M. Albella, J. Phys. Chem. **100**, 2148 (1996)
36. X. Yang, S. Nitta, M. Pristovsek, Y. Liu, Y. Liao, M. Kushimoto, Y. Honda, H. Amano, 2D Mater. **7**, 5004 (2020)
37. V. Kumar, B. Roy, P. Sharma, Int. J. Hydrogen Energy **44**, 22022 (2019)
38. M. Chubarov, H. Högberg, A. Henry, H. Pedersen, J. Vac. Sci. Technol. A **36**, 030801 (2018)